Supporting Information

Metal Selection Tactic in Nitronyl Nitroxide Biradical-3d-4f Macrocycle for Boosting Photothermal Conversion and Application of Solar-Driven Water Evaporation

Hongdao Li*[a,b], Chaoyi Jin[b], Lu Xi,[b] Lifeng Ding,[a] Jing Han[b] and Pei Jing[b]

[a] *Department of Chemistry and Chemical Engineering, Taiyuan Institute of Technology, Taiyuan 030008, China*

[b] *Department of Chemistry, Key Laboratory of Advanced Energy Materials Chemistry and Tianjin Key Laboratory of Metal and Molecule-based Material Chemistry, College of Chemistry, Nankai University, Tianjin 300071, China*

Table of Content

1. Experimental Procedures

Materials and Physical measurements

All the reagents and solvents were commercially available and used as received. FT-IR data were recorded on a Vector27 Bruker Spectrophotometer with KBr pellets in the 4000-400 cm^{-1} region. Elemental analyses for C, H, and N were recorded on a Perkin-Elmer 240C analyzer. The PXRD data were collected on a Bruker Advance D8 diffractometer with Cu radiation (λ = 1.54056 Å) at room temperature. TGA data were obtained on a STA 449C thermal analysis system under N_2 atmosphere. X-Ray photoelectron spectroscopy (XPS) measurements were performed on a Thermo Fisher Scientific ESCALAB Xi+ system with an Al Kα source. UV-Vis-NIR Diffuse reflectance spectra (DRS) were recorded using a UV–Vis–NIR spectrophotometer equipped with an integrating sphere, and BaSO4 powder was used as the reference for the baseline correction.

Photothermal conversion: 270 mg of **DyCo-1**, **YbCo-2** and **DyZn-3** thin round layer (thickness of 1.5 mm) with the largest possible surface area (diameter of 1.5 cm) placed on a tripod at a distance of 20 cm from the 1064 nm laser (0.3 W cm^{-2}). The infrared camera was used to capture the infrared videos of **DyCo-1, YbCo-2 and DyZn-3** samples when the illumination was on/off. The infrared photos and real-time temperatures were extracted from the video.

DyCo-1-loaded polyethylene terephthalate (PET) sample was put on a plastic evaporating dish filled with pure water, surrounded by thermally insulating foam. Sunlight was simulated by a Xenon lamp with an optical filter (AM 1.5 G) and used to irradiate the sample under 0.1 W cm^{-2} power density. The mass change of the water was recorded by an electronic balance (accuracy of 0.00001 g). The IR camera was used to measure the temperature.

Synthesis of bisNITCH$_2$bz

Ligand bisNITCH$_2$bz was synthesized according to the previous method.[S1]

Synthesis of DyCo-1, YbCo-2, DyZn-3 and GdCo-4

Ln(hfac)$_3$·2H$_2$O (0.01 mmol) and M(hfac)$_2$·2H$_2$O (0.01 mmol) was suspended in 25 mL of n-hexane to reflux for 5 hours until most of them dissolved, and a solution of bisNITCH$_2$bz (0.01 mmol) in 6 mL of $CHCl_3$ or CH_2Cl_2 was introduced with stirring. After 30 min, the resulting blue solution was filtered, and the above filtrate store in the refrigerator (0-5 °C) to generate blue crystals.

DyCo-1: Yield 80%. $C_{47}H_{37}CoDyF_{30}N_8O_{14}$ (1729.22 g/mol) (without solvent molecules): calcd. C 32.64, H 2.15, N 6.48; found. C 32.62, H 2.11, N 6.46; FT-IR (KBr): 3147(w), 1652(s), 1502 (m), 1364 (m), 1261 (s), 1203 (s), 1147 (s), 800 (m), 665 (m), 582 (m) cm^{-1}.

YbCo-2: Yield 83%. $C_{47}H_{37}CoYbF_{30}N_8O_{14}$ (1739.76 g/mol) (without solvent molecules): calcd. C 32.44, H 2.14, N 6.44; found. C 32.41, H 2.17, N 6.42; FT-IR (KBr): 3145(w), 1654(s), 1501 (m), 1366 (m), 1260 (s), 1200 (s), 1143 (s), 801 (m), 667 (m), 583 (m) cm^{-1}.

DyZn-3: Yield 81%. $C_{47}H_{37}ZnDyF_{30}N_8O_{14}$ (1735.70 g/mol) (without solvent molecules): calcd. C 32.52, H 2.14, N 6.45; found. C 32.56, H 2.17, N 6.43; FT-IR (KBr): 3145(w), 1652(s), 1502 (m), 1364 (m), 1263 (s), 1200 (s), 1147 (s), 801 (m), 669 (m), 581 (m) cm^{-1}.

GdCo-4: Yield 80%. $C_{47}H_{37}CoGdF_{30}N_8O_{14}$ (1723.97 g/mol) (without solvent molecules): calcd. C 32.74, H 2.16, N 6.49; found. C 32.70, H 2.15, N 6.46; FT-IR (KBr): 3148(w), 1652(s), 1501 (m), 1364 (m), 1265 (s), 1200 (s), 1147 (s), 801 (m), 669 (m), 583 (m) cm^{-1}.

The peak observed at about 1502 cm^{-1} (m, $\nu_{C=N}$) is attributed nitronyl nitroxide ligand. Peaks at about 1265 cm^{-1} (s), 1200 cm^{-1} (s) and 1147 cm^{-1} ($\nu_{C\text{-}F}$) are attributed to the coligand $hfac^-$.

X-ray Crystallography

Single-crystal structure investigations were performed on a Rigaku Saturn diffractometer equipped with a CCD area detector and graphite-monochromated Mo/Kα radiation (λ = 0.71073 Å) at 150 K or 100 K. Empirical absorption corrections based on symmetry equivalent reflections were applied. The structure solution was done with direct methods using SHELXS-2014[S2], and structure refinements were performed by a full-matrix least-squares procedure using SHELXL-2014[S3]. Anisotropic thermal parameters were assigned to all non-hydrogen atoms. Hydrogen atoms were placed in calculated, ideal positions and were refined isotropically as riding on their respective C atoms. For **YbCo-2** and **GdCo-4**, the SQUEEZE option in PLATON[S4] was used to remove the disordered solvent water molecules. CCDC 2419394-2419397 contain the supplementary crystallographic data for this paper. These data can be obtained free of charge from The Cambridge Crystallographic Data Centre.

2. Supporting Tables

Table S1. The crystal data and refinement details of **1** and **2**.

Complex	**1**	**2**
Empirical formula	$C_{101}H_{89}Cl_3Co_2Dy_2F_{60}N_{16}O_{28}$	$C_{95}H_{75}Cl_3Co_2Yb_2F_{60}N_{16}O_{28}$
Mr	3664.0	3598.91
T (K)	150.0	100.15
Crystal system	monoclinic	monoclinic
Space group	$P2_1/c$	$P2_1/c$
a /Å	17.1476(5)	16.9980(4)
b /Å	22.0824(7)	22.0568(4)
c /Å	19.8106(6)	19.4263(4)
α /º	90	90
β /º	108.3030(10)	106.823(2)
γ /º	90	90
V /Å^3	7122.0(4)	6971.6(3)
Z	4	4
D_{calcd} /g cm^{-3}	1.764	1.771
θ /º	2.502-52.772	6.744-60.848
F(000)	3732	3648
Reflections collected	64388	62116
Unique reflns/R_{int}	14586/0.0638	21122/0.0367
GOF (F^2)	1.041	1.036
R_1, wR_2 ($I > 2\sigma(I)$)	0.0672, 0.1957	0.0572, 0.1629
R_1, wR_2 (all data)	0.0772, 0.2023	0.0760, 0.1795

Table S2. The crystal data and refinement details of **3** and **4**.

Complex	**3**	**4**
Empirical formula	$C_{96}H_{78}Cl_4Zn_2Dy_2F_{60}N_{16}O_{28}$	$C_{101}H_{89}Cl_3Co_2Gd_2F_{60}N_{16}O_{28}$
Mr	3641.27	3653.50
T (K)	150.0	100.15
Crystal system	monoclinic	monoclinic
Space group	$P2_1/n$	$P2_1/c$
a /Å	19.843(3)	17.2859(3)
b /Å	12.246(2)	21.9920(4)
c /Å	29.537(5)	19.1401(4)
α /º	90	90
β /º	103.231(6)	106.412(2)
γ /º	90	90
V /Å^3	6987.2(19)	6979.7(2)
Z	4	4
D_{calcd} /g cm^{-3}	1.811	1.754
θ /º	2.796-53.242	7.104-61.292
F(000)	3748.0	3624
Reflections collected	96805	47969
Unique reflns/R_{int}	14676/0.0859	21578/0.0480
GOF (F^2)	0.950	0.961
R_1, wR_2 ($I > 2\sigma(I)$)	0.0934, 0.2404	0.0554, 0.1521
R_1, wR_2 (all data)	0.1048, 0.2480	0.0807, 0.1729

Table S3. The important bond lengths [Å] and angles [°] for **1** and **2**.

Complex	**1**	**2**
Ln-O(rad)	2.337(4), 2.339(5)	2.286(4), 2.301(4)
Ln-O(hfac)	2.340(5)-2.386(5)	2.294(4)-2.343(4)
Co-N	2.165(5), 2.112(5)	2.154(4), 2.108(4)
Co-O(hfac)	2.043(5)-2.106(5)	2.042(4)-2.101(4)
O(rad)-Ln-O(rad)	138.30(18)	137.14(15)
N-Co-N	97.9(2)	97.47(17)

Table S4. The important bond lengths [Å] and angles [°] for **3** and **4**.

Complex	**3**	**4**
Ln-O(rad)	2.337(6), 2.288(6)	2.341(3), 2.367(3)
Ln-O(hfac)	2.322(6)-2.375(6)	2.371(3)-2.394(3)
Zn(Co)-N	2.104(7), 2.126(8)	2.141(4), 2.100(4)
Zn(Co)-O(hfac)	2.054(7)-2.129(7)	2.045(3)-2.100(3)
O(rad)-Ln-O(rad)	137.5(2)	139.33(12)
N-Zn(Co)-N	96.5(3)	96.93(14)

Table S5. SHAPE analysis of Ln^{III} ion for complexes **1-4**.

	SAPR-8	TDD-8	BTPR-8
1-Dy	2.231	**0.257**	2.518
2-Yb	2.101	**0.252**	2.458
3-Dy	1.538	**0.327**	2.154
4-Gd	2.079	**0.381**	2.225

SAPR-8 (D_{4d}): Square antiprism; TDD-8 (D_{2d}): Triangular dodecahedron; BTPR-8 (C_{2v}): Biaugmented trigonal prism

3. Supporting Figures

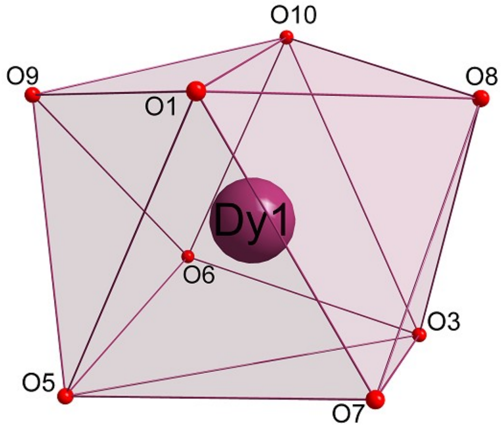

Fig. S1. Coordination environment of the Dy^{III} ion in compound **DyCo-1**.

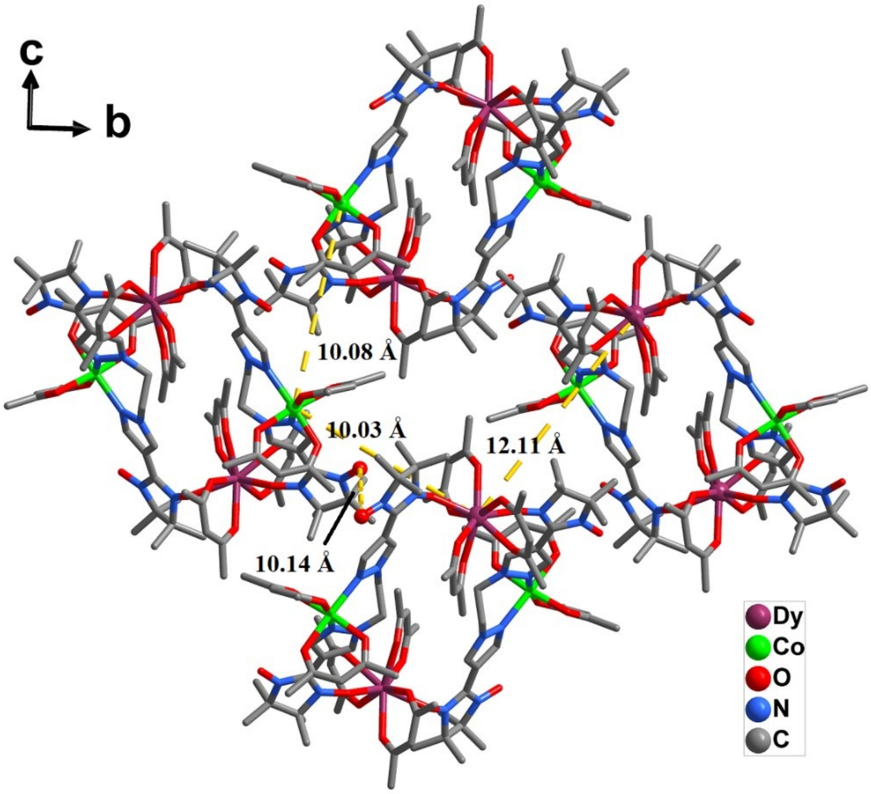

Fig. S2. Molecular packing along the *a*-axis direction for **DyCo-1**. Free solvent molecules, H and F atoms have been omitted.

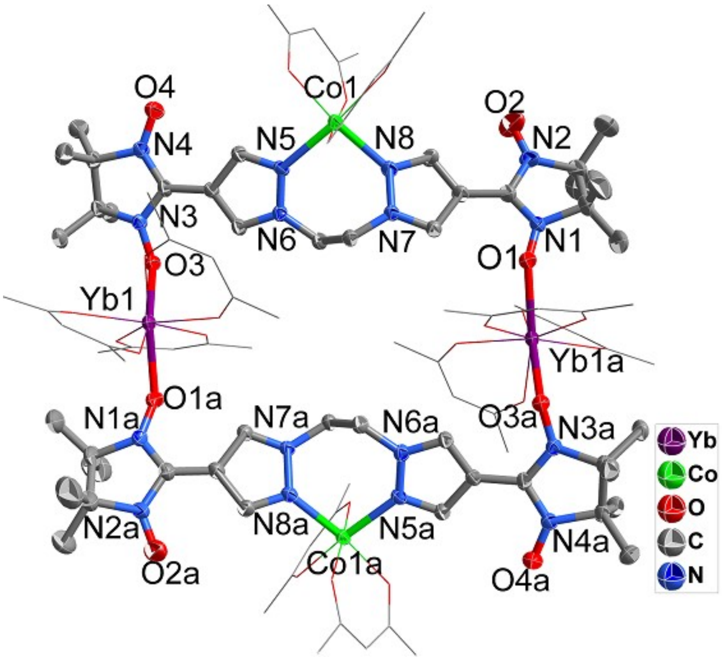

Fig. S3. Molecular structure for **YbCo-2**. Free solvent molecules, H and F atoms have been omitted.

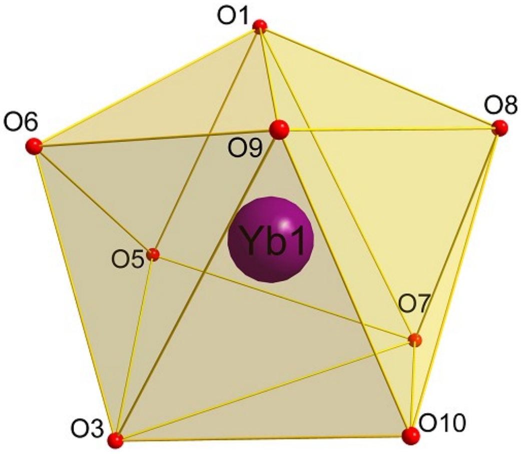

Fig. S4. Coordination environment of the Yb^{III} ion in compound **YbCo-2**.

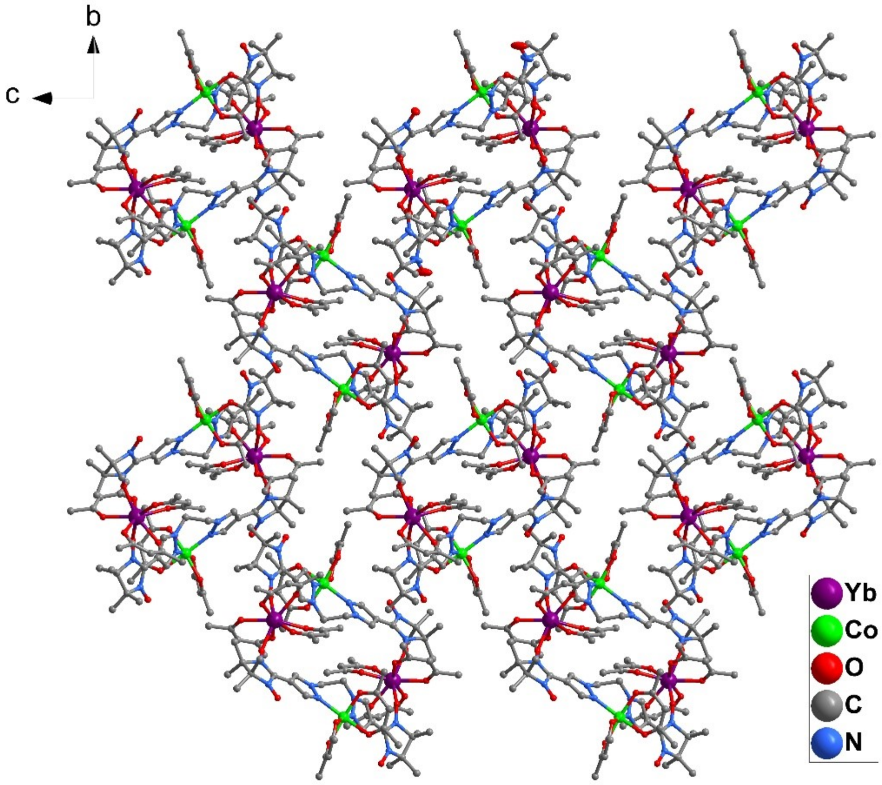

Fig. S5. Molecular packing along the *a*-axis direction for **YbCo-2**. Free solvent molecules, H and F atoms have been omitted.

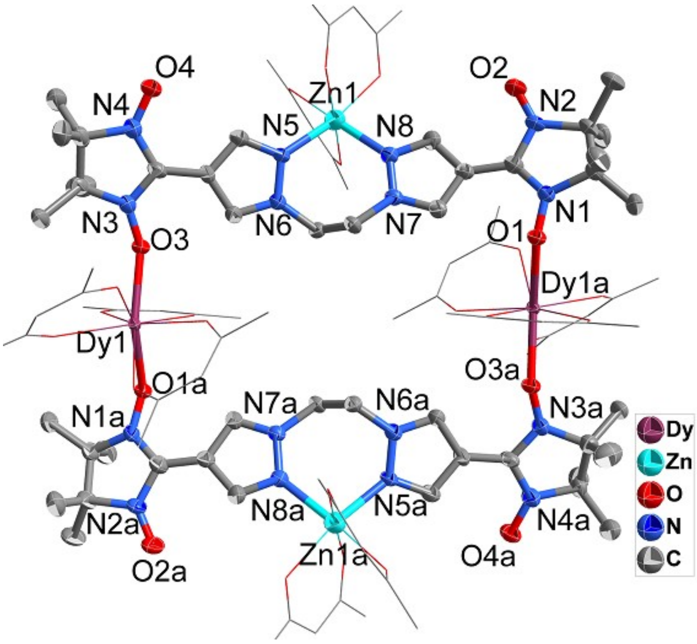

Fig. S6. Molecular structure for **DyZn-3**. Free solvent molecules, H and F atoms have been omitted.

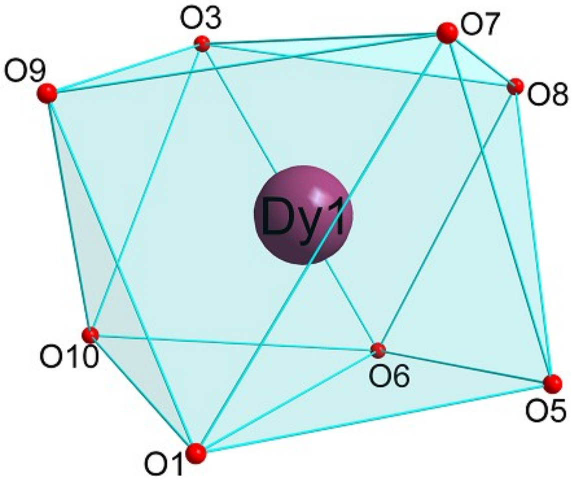

Fig. S7. Coordination environment of the Dy^{III} ion in compound **DyZn-3**.

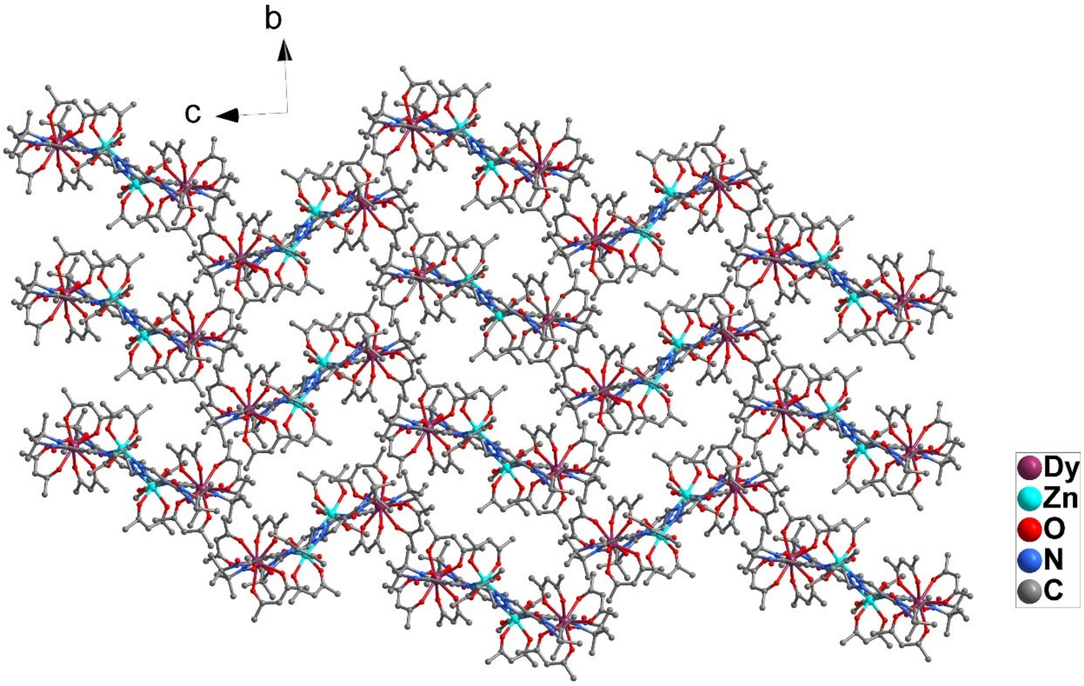

Fig. S8. Molecular packing along the *a*-axis direction for **DyZn-3**. Free solvent molecules, H and F atoms have been omitted.

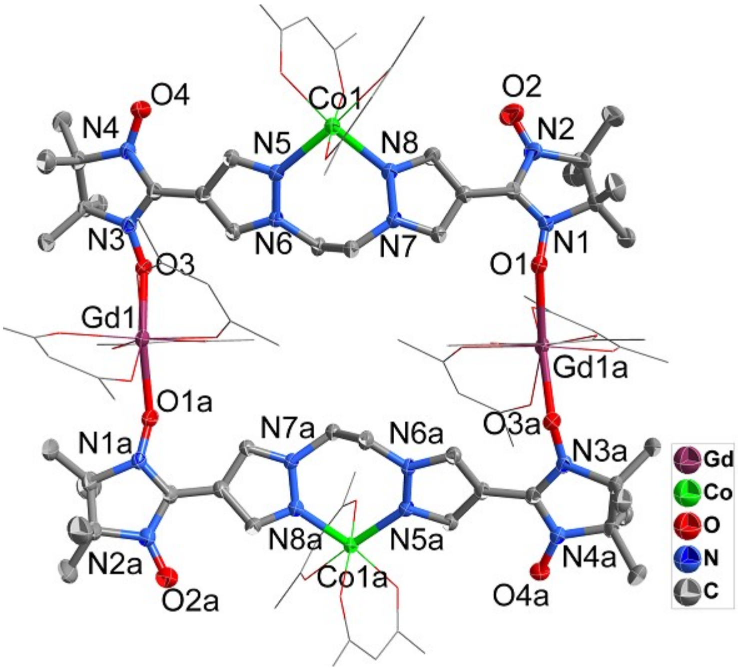

Fig. S9. Molecular structure for **GdCo-4**. Free solvent molecules, H and F atoms have been omitted.

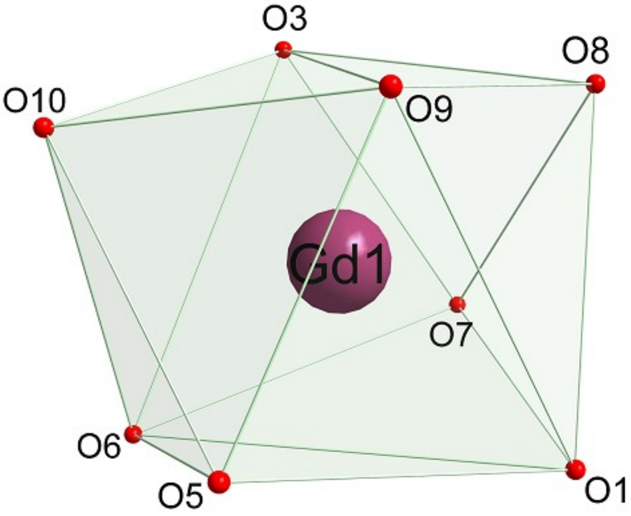

Fig. S10. Coordination environment of the Gd^{III} ion in compound **GdCo-4**.

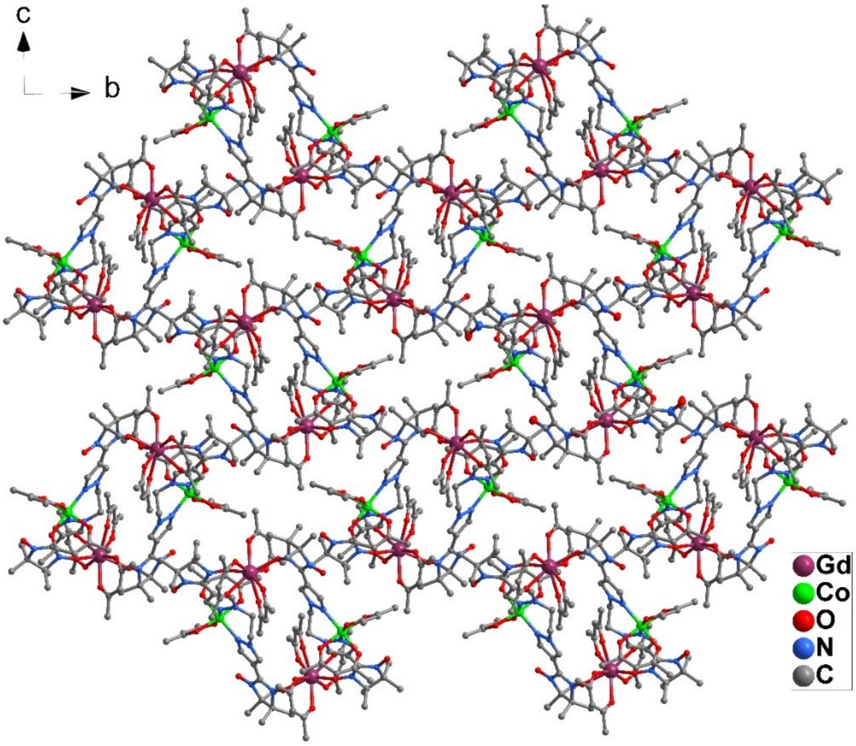

Fig. S11. Molecular packing along the *a*-axis direction for **GdCo-4**. Free solvent molecules, H and F atoms have been omitted.

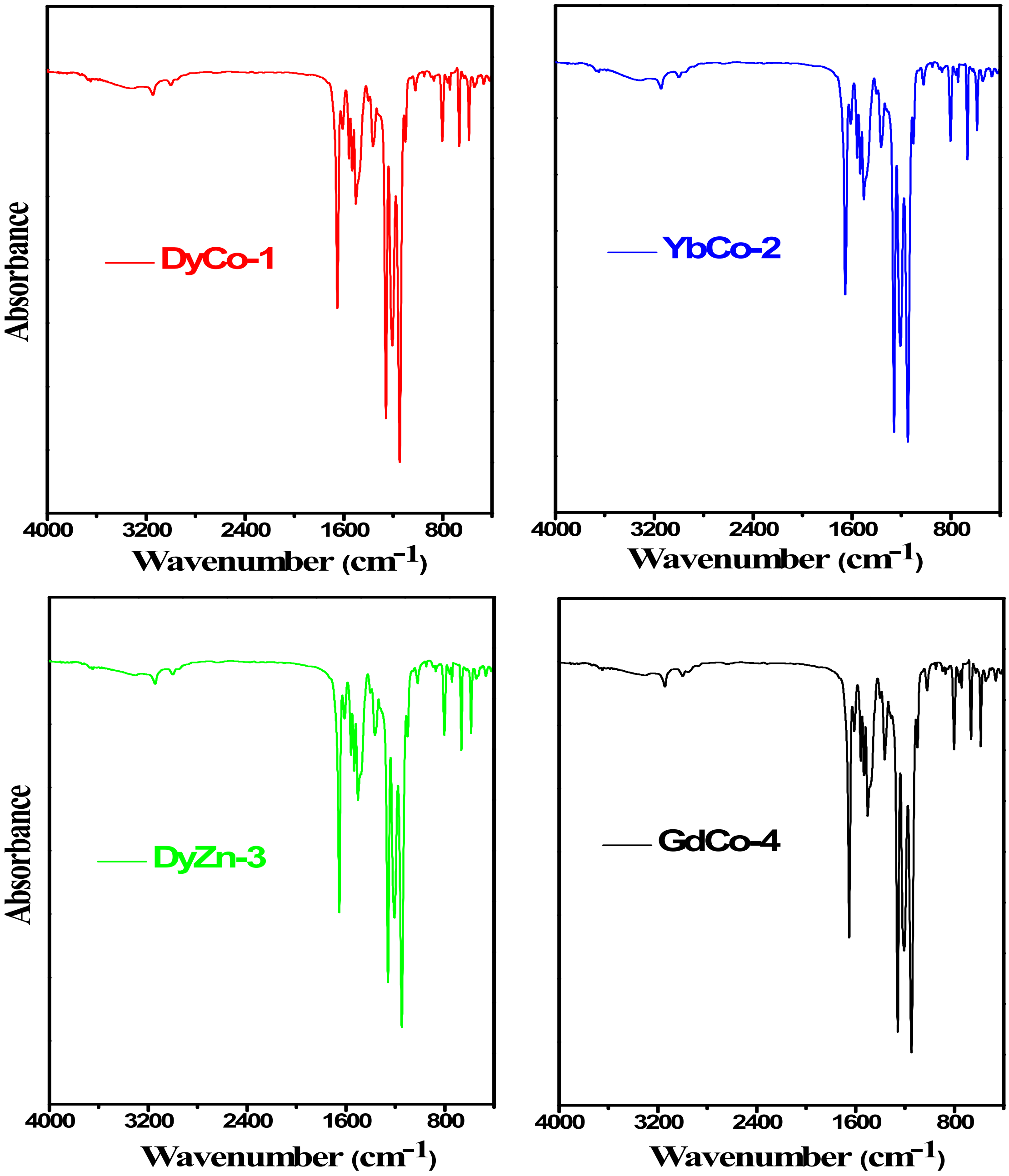

Fig. S12. Infrared spectra of complexes **DyCo-1**, **YbCo-2**, **DyZn-3** and **GdCo-4**.

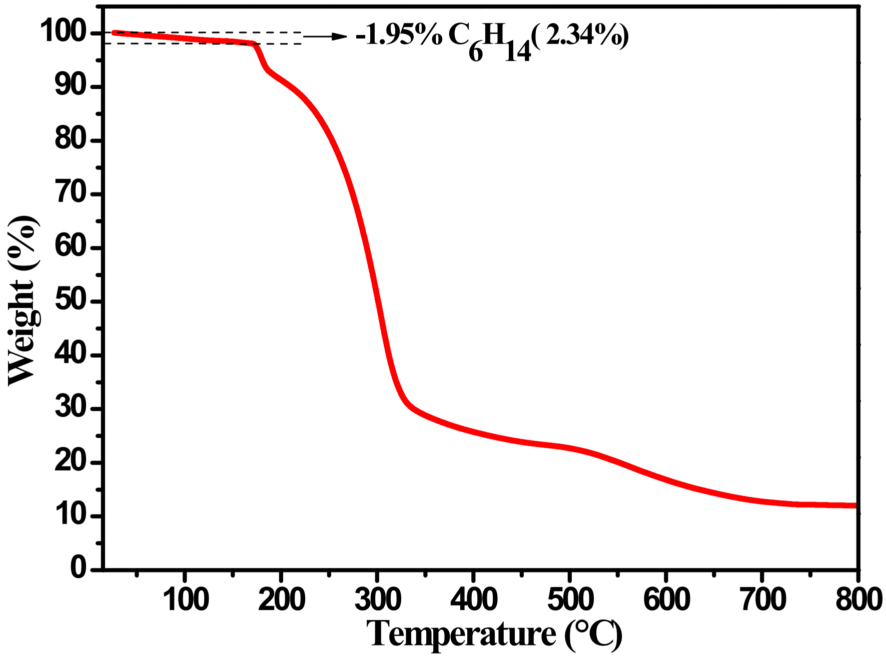

Fig. S13. Thermogravimetric curves of **DyCo-1** in N_2 atmosphere.

Thermogravimetric analysis was conducted from room temperature to 800 °C under N_2 atmosphere. A plateau up to ca. 172 °C, then, **DyCo-1** began to decompose. Since the $CHCl_3$ solvent is extremely volatile and has been volatilized before the thermogravimetric test, no weight loss was detected.

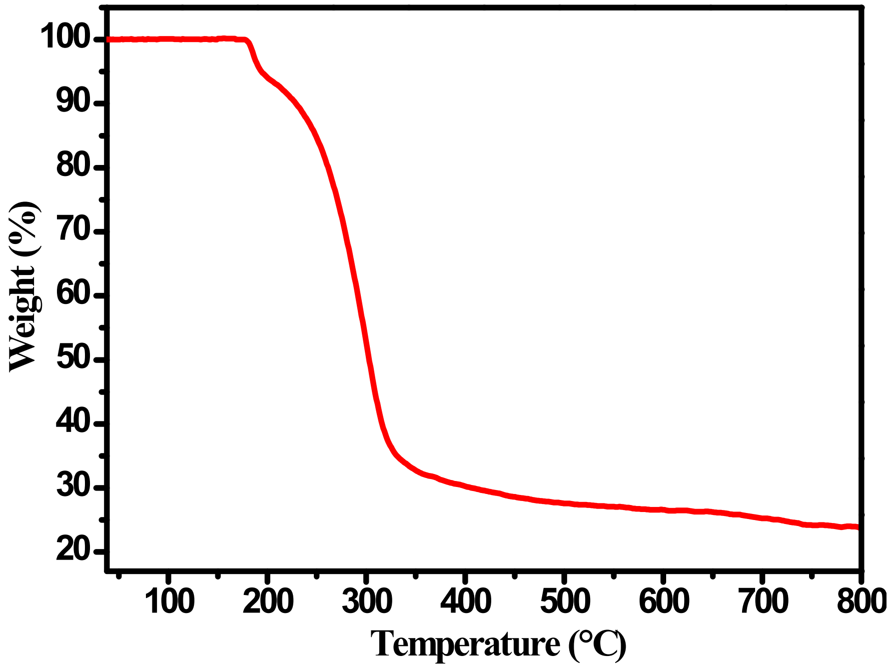

Fig. S14. Thermogravimetric curves of **YbCo-2** in N_2 atmosphere.

Thermogravimetric analysis was conducted from room temperature to 800 °C under N_2 atmosphere. A plateau up to ca. 177 °C, then, **YbCo-2** began to decompose. Since the $CHCl_3$ solvent is extremely volatile and has been volatilized before the thermogravimetric test, no weight loss was detected.

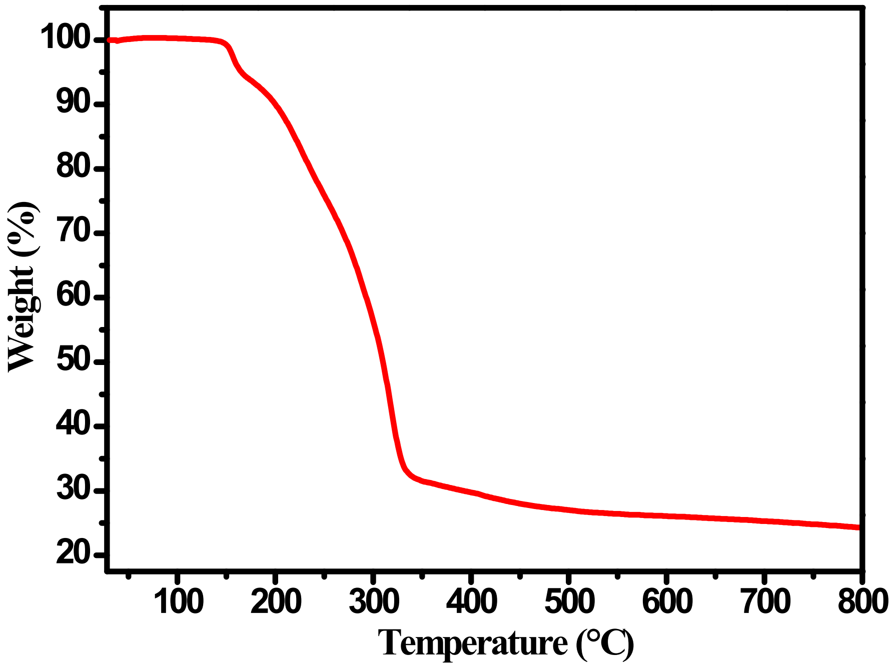

Fig. S15. Thermogravimetric curves of **DyZn-3** in N_2 atmosphere.

Thermogravimetric analysis was conducted from room temperature to 800 °C under N_2 atmosphere. A plateau up to ca. 150 °C, then, **DyZn-3** began to decompose. Since the CH_2Cl_2 solvent is extremely volatile and has been volatilized before the thermogravimetric test, no weight loss was detected.

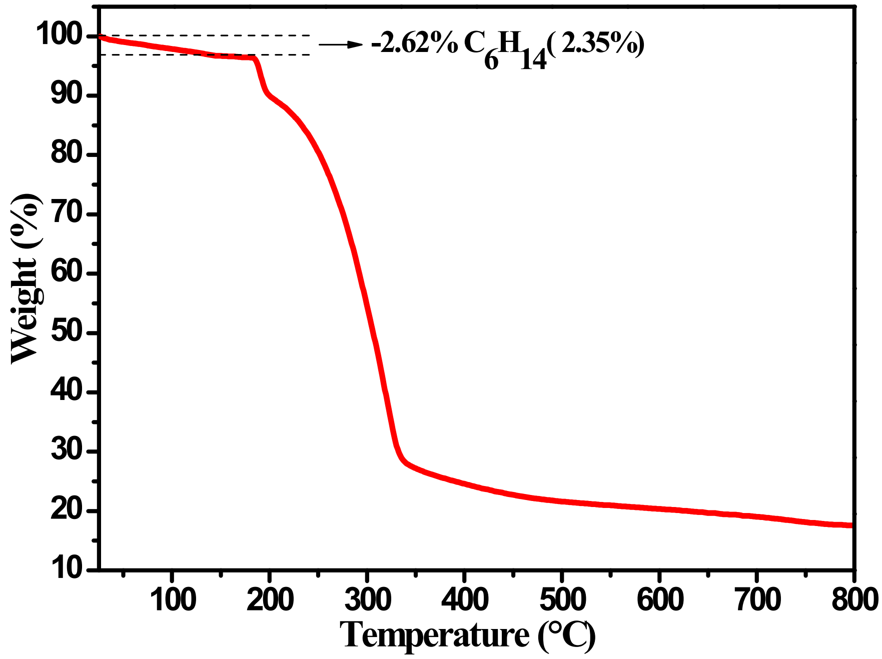

Fig. S16. Thermogravimetric curves of **GdCo-4** in N_2 atmosphere.

Thermogravimetric analysis was conducted from room temperature to 800 °C under N_2 atmosphere. A plateau up to ca. 184 °C, then, **GdCo-4** began to decompose. Since the $CHCl_3$ solvent is extremely volatile and has been volatilized before the thermogravimetric test, no weight loss was detected.

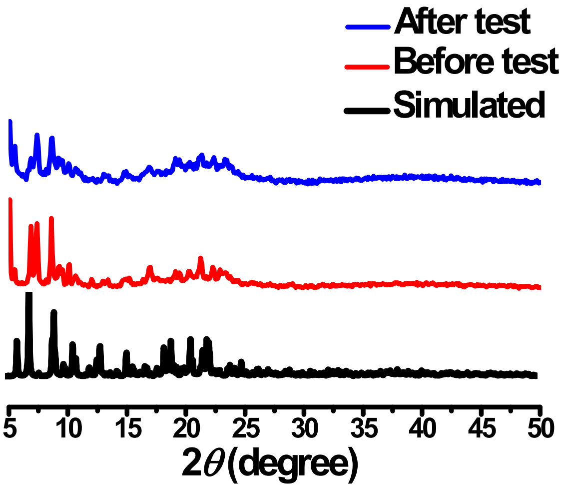

Fig. S17. PXRD patterns of **DyCo-1** theoretical parameter, before and after the photothermal water evaporation.

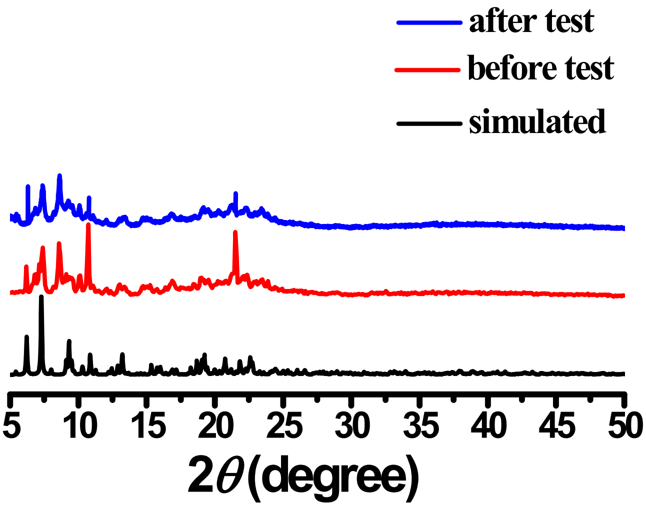

Fig. S18. PXRD patterns of **YbCo-2** theoretical parameter, before and after the photothermal test.

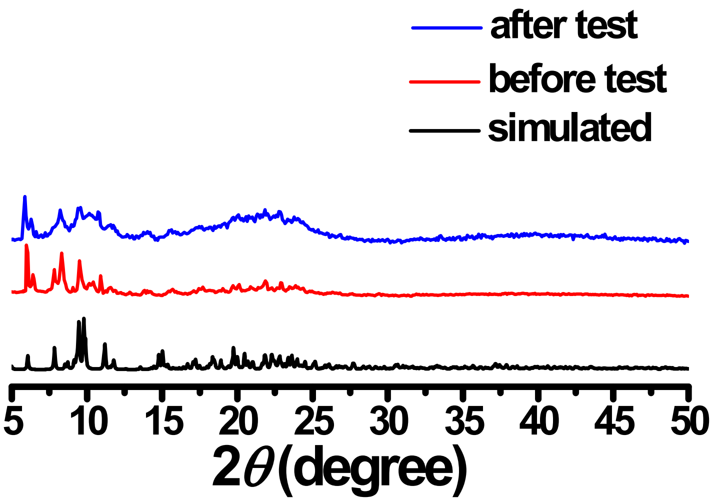

Fig. S19. PXRD patterns of **DyZn-3** theoretical parameter, before and after the photothermal test.

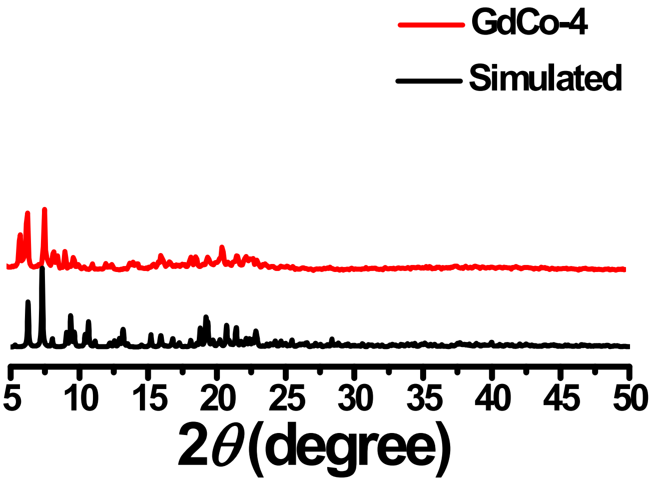

Fig. S20. Powder X-ray diffraction patterns of **GdCo-4.**

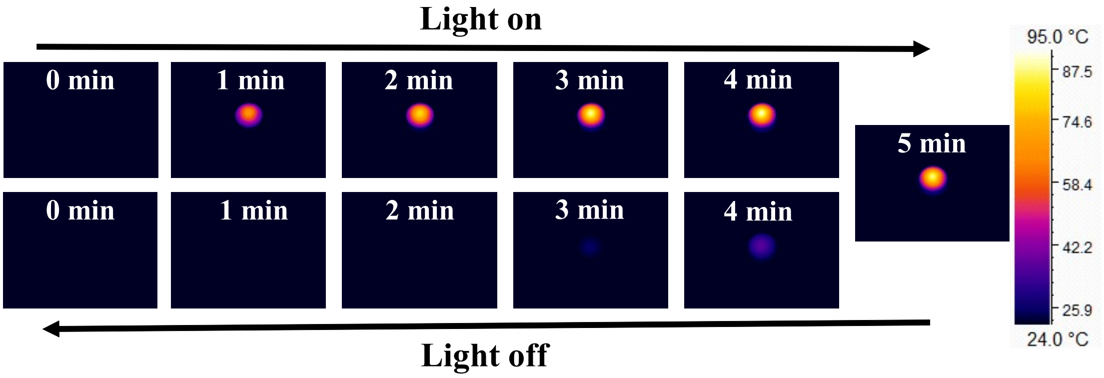

Fig. S21. IR thermal images of **YbCo-2** under on and off irradiation of 1064 nm (0.3 W cm^{-2}) laser.

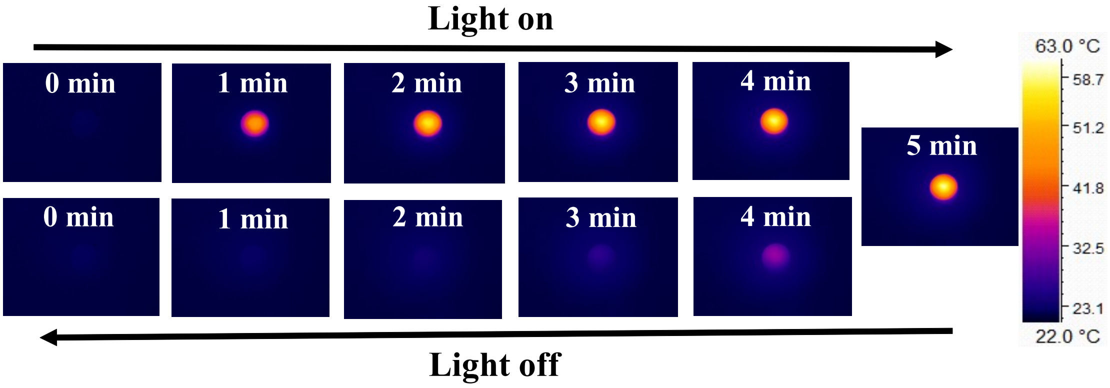

Fig. S22. IR thermal images of **DyZn-3** under on and off irradiation of 1064 nm (0.3 W cm^{-2}) laser.

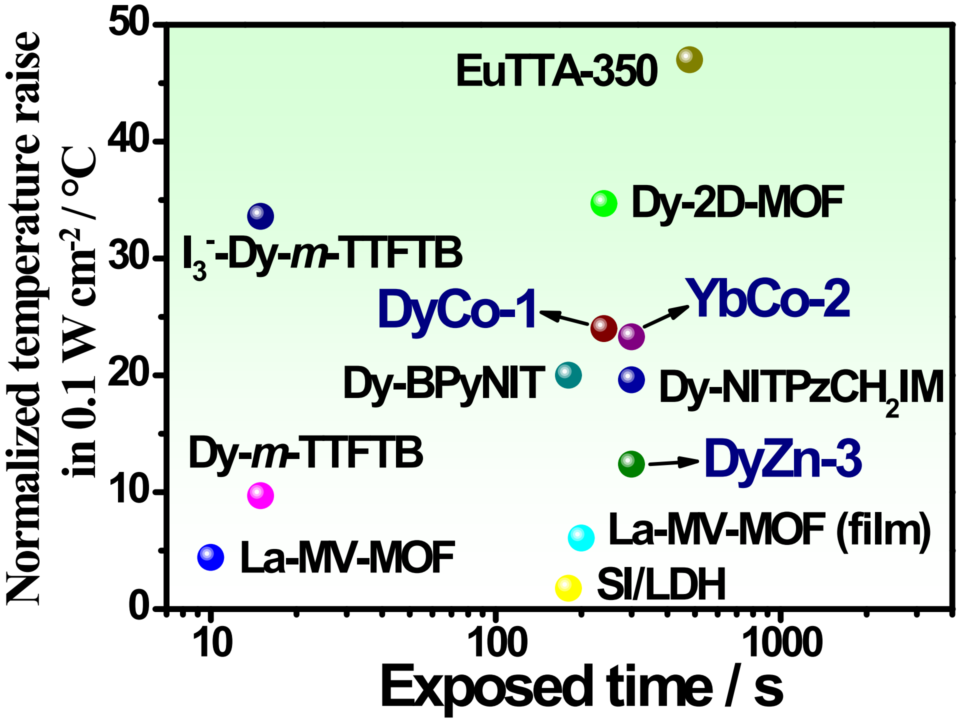

Fig. S23. The temperature increment of lanthanide-functional ligand photothermal materials normalized by one unit sunlight.

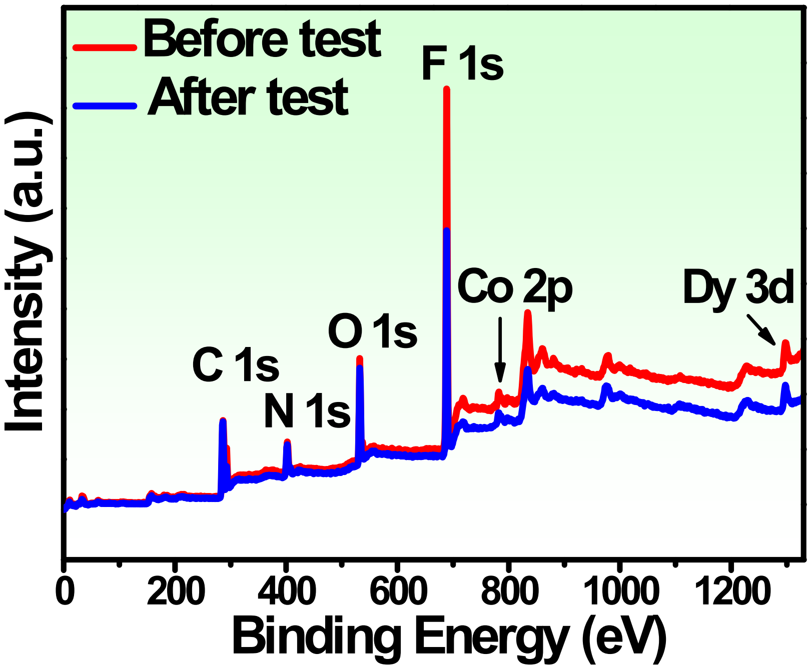

Fig. S24. XPS spectra of **DyCo-1** before and after the photothermal test.

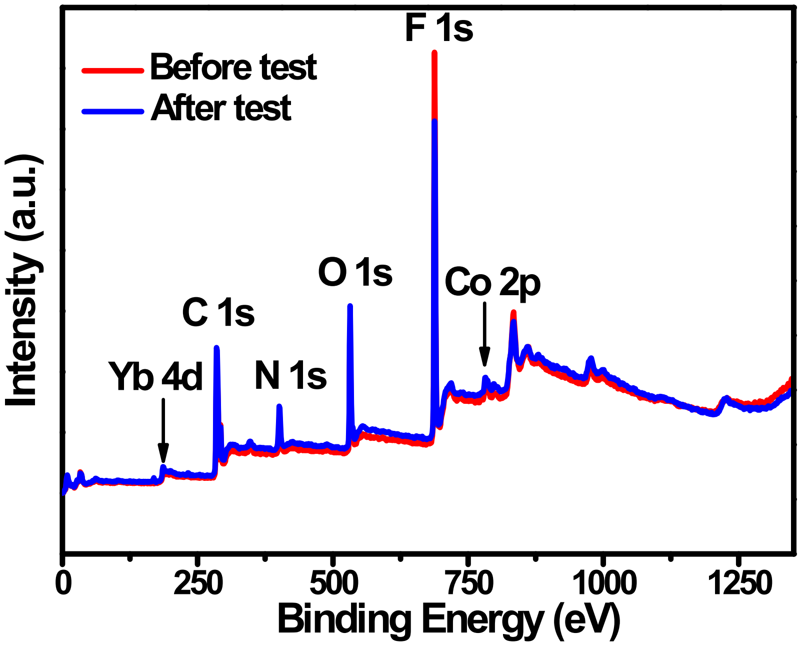

Fig. S25. XPS spectra of **YbCo-2** before and after the photothermal test.

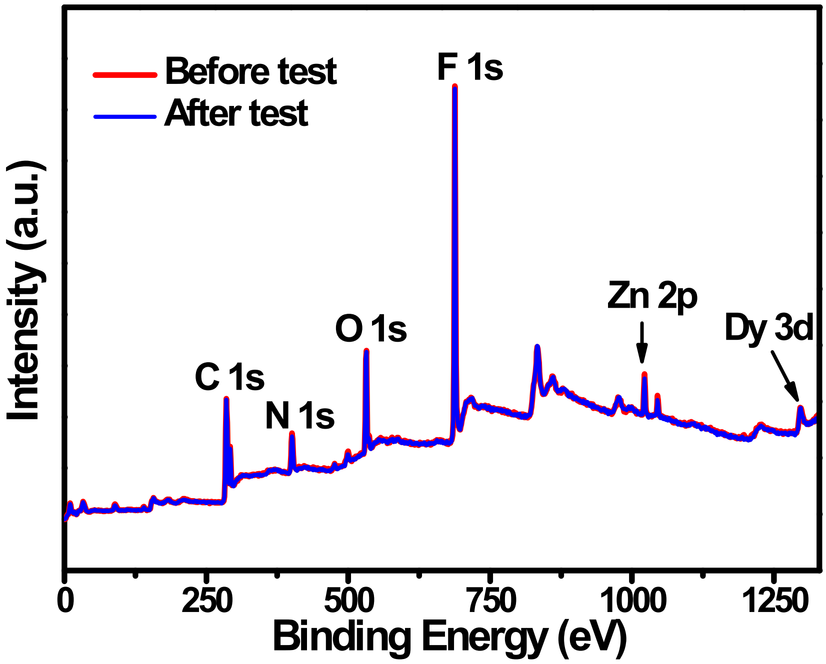

Fig. 26. XPS spectra of **DyZn-3** before and after the photothermal test.

4. Photothermal conversion efficiency calculation

The conversion efficiency was determined according to previous method[S16]. Details are as follows: Based on the total energy balance for this system:

$$\sum_i m_i C_{pi} \frac{dT}{dt} = Q_s - Q_{loss}$$

where m_i (0.270 g) and $C_{p,i}$ (0.8 J (g°C) $^{-1}$) are the mass and heat capacity of system components, respectively. Q_s is the photothermal heat energy input by irradiating NIR laser to samples, and Q_{loss} is thermal energy lost to the surroundings. When the temperature is maximum, the system is in balance.

$$Q_s = Q_{loss} = hS\Delta T_{max}$$

where h is heat transfer coefficient, S is the surface area of the container, $\Delta T_{\max}$ is the maximum temperature change. The photothermal conversion efficiency η is calculated from the following equation:

$$\eta = \frac{hS\Delta T_{max}}{I(1-10^{-A_{1064}})}$$

where I is the laser power (power density, 0.3 W cm^{-2}) and A_{1064} is the absorbance of the sample (0.27 g) at the wavelength of 1064 nm (**DyCo-1**: $A'_{1064} = 0.241$; **YbCo-2**: $A'_{1064} = 0.166$; **DyZn-3**: $A'_{1064} = 0.063$; m*'*: 0.027 g). In order to obtain the *hS*, a dimensionless driving force temperature, θ is introduced as follows:

$$\theta = \frac{T - T_{surr}}{T_{max} - T_{surr}}$$

where T is the temperature of sample, $T_{\max}$ is the maximum system temperature, and T_{surr} is the initial temperature.

The sample system time constant τs:

$$\tau_s = \frac{\sum_i m_i C_{p,i}}{hS}$$

thus $\frac{d\theta}{dt} = \frac{1}{\tau_s}\frac{Q_s}{hS\Delta T_{max}} - \frac{\theta}{\tau_s}$

when the laser is off, Qs = 0, therefore $\frac{d\theta}{dt} = -\frac{\theta}{\tau_s}$,and $t = -\tau_s \ln\theta$

so *hS* could be calculated from the slope of cooling time vs ln*θ*.

The detailed calculation results of each parameter are shown in the following table.

Table S6. The detailed calculation results of photothermal conversion efficiency η.

	A	T_{surr} / °C	$T_{\max}$ / °C	τ_s / S	*hS*	η
DyCo-1	2.41	24.2	96.3	68.87	0.00313	75.5%
YbCo-2	1.66	20.2	90.0	69.8	0.00302	71.9%
DyZn-3	0.63	23.8	61.2	61.23	0.00352	57.3%

Table S7. Photothermal property in this work compared with previous reported solid lanthanide/transition metal-based materials.

Samples	**Light source**	**Light Intensity**	**Added temperature**	**Normalized temperature raise in 0.1 W cm^{-2}**	η	**Ref**
DyCo–bisNITCH$_2$bz	1064 nm laser	0.3 W cm^{-2}	72.0 °C in 4 min	24.0 °C in 4 min	75.5 %	**This work**
YbCo–bisNITCH$_2$bz	1064 nm laser	0.3 W cm^{-2}	67.8 °C in 5 min	22.6 °C in 5 min	71.9 %	
DyZn–bisNITCH$_2$bz	1064 nm laser	0.3 W cm^{-2}	37.4 °C in 5 min	12.4 °C in 5 min	57.3 %	
Dy-BPyNIT	1064 nm laser	0.1 W cm^{-2}	20.0 °C in 3 min	20.0 °C in 3 min	74.1 %	[S5]
Dy-NITPzCH$_2$IM	1064 nm laser	0.1 W cm^{-2}	19.6 °C in 5 min	19.6 °C in 5 min	56.9 %	[S5]
YbL@MSN	690 nm laser	0.7 W cm^{-2}	23.0 °C in 900 s	3.28 °C in 900 s	45 %	[S6]
La-MV-MOF(film)	808 nm laser	2 W cm^{-2}	121.9 °C in 200 s	6.08 °C in 200 s	77 %	[S7]
La-MV-MOF(cryst)	808 nm laser	2 W cm^{-2}	88 °C in 10 s	4.4 °C in 10 s	--	[S7]
Ag(TEPE)](AC)	808 nm laser	1 W cm^{-2}	134.7 °C in 30 s	13.4 °C in 30 s	51.8 %	[S8]
Ag(TEPE)](NC)	808 nm laser	1 W cm^{-2}	87.2 °C in 40 s	8.7 °C in 40 s	36.2 %	[S8]
Dy-2D-MOF	1 sun light	0.1 W cm^{-2}	34.7 °C in 4 min	34.7 °C in 4 min	--	[S9]
Dy-*m*-TTFTB	808 nm laser	0.1 W cm^{-2}	9.7 °C in 15 s	9.7 °C in 15 s	--	[S10]
I$_3^-$Dy-*m*-TTFTB	808 nm laser	0.1 W cm^{-2}	33.6 °C in 15 s	33.6 °C in 15 s	--	[S10]
S&I/LDH	808 nm laser	0.5 W cm^{-2}	8.8 °C in 3 min	1.76 °C in 3 min	--	[S11]
EuTTA-350	420-2500 nm	0.1 W cm^{-2}	47 °C in 480 s	47 °C in 480 s	--	[S12]
HKUST-1	300-650 nm	0.5 W cm^{-2}	99.3 °C in 30 min	19.86 °C in 30 min	33.6 %	[S13]
UiO-66	300-650 nm	0.5 W cm^{-2}	31.8 °C in 30 min	6.36 °C in 30 min	5 %	[S13]
UiO-66-NH$_2$	300-650 nm	0.5 W cm^{-2}	123.6 °C in 30 min	24.72 °C in 30 min	59.3 %	[S13]
ZIF-8	300-650 nm	0.5 W cm^{-2}	44.4 °C in 30 min	8.88 °C in 30 min	0.3 %	[S13]
ZIF-67	300-650 nm	0.5 W cm^{-2}	101.3 °C in 30 min	20.26 °C in 30 min	50 %	[S13]
Fe-MIL-NH$_2$	300-650 nm	0.5 W cm^{-2}	115.8 °C in 30 min	23.16 °C in 30 min	86.6 %	[S13]
IR-MOF-3	300-650 nm	0.5 W cm^{-2}	92.2 °C in 30 min	18.44 °C in 30 min	25.8 %	[S13]
CPO-27-Mg	300-650 nm	0.5 W cm^{-2}	111.7 °C in 30 min	22.34 °C in 30 min	21.6 %	[S13]
THPTS-Pb	1064 nm laser	0.8 W cm^{-2}	64 °C in 180 s	8 °C in 180 s	15.2 %	[S14]
Ag-2D-CPs	800 nm laser	0.5 W cm^{-2}	24.5 °C in 3 min	4.9 °C in 3 min	22.1 %	[S15]

Assumption of the added temperature is in direct proportion to light intensity for approximate comparison. This column will give the value of the normalized temperature raise for these materials irradiated with the light of 0.1 W cm^{-2}. The raised temperatures were recorded when samples reached the steady-state, in which the temperature hardly raises by further illumination. η: photothermal conversion efficiency

5. Solar-driven water evaporation efficiency calculation

The efficiency (η) was calculated based on the following equation[S17]:

$$\eta = mh_{\mathrm{LV}}/C_{\mathrm{opt}}P_0$$

where m refers to the mass flux (evaporation rate) of water, h_{LV} refers to the total liquid-vapor phase-change enthalpy (i.e., the sensible heat and the enthalpy of evaporation $h_{\mathrm{LV}} = Q + \Delta h_{\mathrm{vap}}$), Q is the energy consumption to heat the system from the initial temperature T_0 to the final temperature T, Δh_{vap} is the latent heat of evaporation of water. And t is the normalized irradiation time (3600 s), P_0 is the normalized solar irradiation value of 1 kW m^{-2}, and C_{opt} represents the optical concentration.

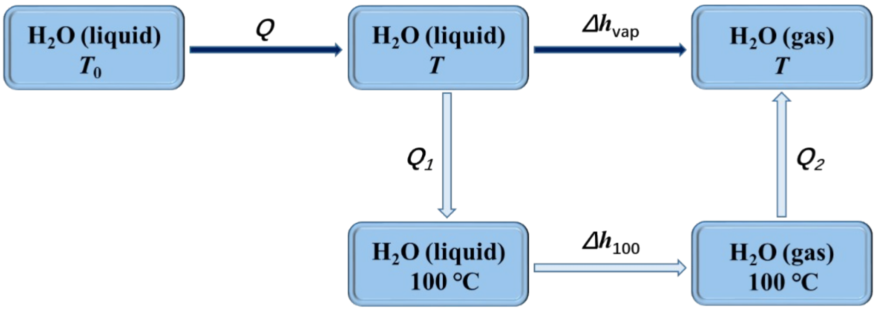

$$Q = C_{\mathrm{liquid}} \times (T - T_0)$$

$$\Delta h_{\mathrm{vap}} = Q_1 + \Delta h_{100} + Q_2$$

$$Q_1 = C_{\mathrm{liquid}} \times (100°\mathrm{C} - T)$$

$$Q_2 = C_{\mathrm{vapor}} \times (T - 100°\mathrm{C})$$

In the experiment, C_{liquid}, the specific heat capacity of water is a constant of 4.18 J g^{-1} °C^{-1}. C_{vapor}, the specific heat capacity of vapor is a constant of 1.865 J g^{-1} °C^{-1}. Δh_{100} is the latent heat of evaporation of water at 100 °C, taken to be 2260 kJ kg^{-1}.

The surface temperature of DyCo-1-loaded PET was 42.8 °C (T) during the evaporation process. According to the above formulas,

$$Q = C_{\mathrm{liquid}} \times (T - T_0) = 4.18 \times (42.8 - 23.2) = 81.93 \text{ kJ kg}^{-1}$$

$$\Delta h_{\mathrm{vap}} = Q_1 + \Delta h_{100} + Q_2 = 4.18 \times (100 - 42.8) + 2260 + 1.865 \times (42.8 - 100) = 2392.41 \text{ kJ kg}^{-1}$$

$$\Delta h_{\mathrm{LV}} = Q + \Delta h_{\mathrm{vap}} = 81.93 + 2392.41 = 2474.34 \text{ kJ kg}^{-1}$$

$\boldsymbol{m} = 0.7728\ \mathrm{kg\ m^{-2}\ h^{-1}}$

$\boldsymbol{t} = 3600\ \mathrm{s}$

$\boldsymbol{P_0} = 1\ \mathrm{kW\ m^{-2}}$

$\boldsymbol{C_{\mathrm{opt}}} = 1$

$\boldsymbol{\eta = m h_{\mathrm{LV}}/C_{\mathrm{opt}} P_0} = 53.1\ \%$

6. References

[S1] E. F. Ullman, L. Call, J. H. Osiecki, Stable free radicals. VIII. New imino, amidino, and carbamoyl nitroxides. *J. Org. Chem.* 1970, **35**, 3623-3631.

[S2] G. M. Sheldrick, SHELXS-2014, Program for Structure Solution; Universitat of Göttingen: Germany, 2014.

[S3] G. M. Sheldrick, SHELXL-2014, Program for Structure Reffnement; Universitat of Göttingen: Germany, 2014.

[S4] A. L. Spek, PLATON-94 (V-101094), A Multipurpose Crystallographic Tool, University of Utrecht, The Netherlands, 1994.

[S5] H. D. Li, C. Y. Jin, J. Han, J. K. Tang, X. F. Han, Z. J. Song, Near-infrared-II photothermal conversion and magnetic dynamic regulation in [$\mathrm{Ln_3Rad_2}$] aggregation by rigidity modification of nitronyl nitroxide. *Inorg. Chem. Front.* 2024, **11**, 8421-8430.

[S6] M. L. Zhu, H. Zhang, G. L. Ran, D. N. Mangel, Y. H. Yao, R. J. Zhang, J. Tan, W. K. Zhang, J. X. Song, J. L. Sessler, J. L. Zhang, Metal modulation: an easy-to-implement tactic for tuning lanthanide phototheranostics. *J. Am. Chem. Soc.* 2021, **143**, 7541-7552.

[S7] S. Wang, S. Li, J. Xiong, Z. Lin, W. Wei, Y. Xu, Near-infrared photothermal conversion of stable radicals photoinduced from a viologen-based coordination polymer. *Chem. Commun.* 2020, **56**, 7399-7402.

[S8] P. Y. Liao, J. X. Li, J. C. Liu, Q. Xiong, Z. Y. Ruan, T. Li, W. Deng, S. D. Jiang, J. H. Jia, M. L. Tong, Radical-Induced Photochromic Silver(I) Metal-Organic Frameworks: Alternative Topology, Dynamic Photoluminescence and Efficient Photothermal Conversion Modulated by Anionic Guests. *Angew. Chem. Int. Ed.* 2024, **136**, e202401448.

[S9] J. Su, N. Xu, R. Murase, Z. M. Yang, D. M. DQAlessandro, J. L. Zuo, J. Zhu, Persistent Radical Tetrathiafulvalene-Based 2D Metal-Organic Frameworks and Their Application in Efficient Photothermal Conversion. *Angew. Chem. Int. Ed.* 2021, **60**, 4789-4795.

[S10] J. Su, P. Y. Cai, T. Yan, Z. M. Yang, S. Yuan, J. L. Zuo, H. C. Zhou, Enhancing the photothermal conversion of tetrathiafulvalene-based MOFs by redox doping and plasmon resonance. *Chem. Sci.* 2022, **13**, 1657-1664.

[S11] X. Mei, J. L. Ma, X. Bai, X. Zhang, S. M. Zhang, R. Z. Liang, M. Wei, D. G. Evans, X. Duan, A bottom-up synthesis of rare-earth-hydrotalcite monolayer nanosheets toward multimode imaging and synergetic therapy. *Chem. Sci.* 2018, **9**, 5630-5639.

[S12] X. H. Ye, L. H. Chung, K. Li, S. Zheng, Y. L. Wong, Z. H. Feng, Y. H. He, D. Chu, Z. T. Xu, L. Yu, J. He, Organic radicals stabilization above 300° C in Eu-based coordination polymers for solar steam generation. *Nat Commun.* 2022, **13**, 6116.

[S13] J. Espin, L. Garzon-Tovar, A. Carne-Sanchez, I. Imaz, D. Maspoch, Photothermal activation of metal–organic frameworks using a UV-vis light source. *ACS Appl. Mater. Interfaces.* 2018, **10**, 9555-9562.

[S14] J. Z. Liao, Z. C. Zhu, S. T. Liu, H. Ke, Photothermal Conversion Perylene-Based Metal-Organic Framework with Panchromatic Absorption Bandwidth across the Visible to Near-Infrared. *Inorg. Chem.* 2024, **63**, 3327-3334.

[S15] M. Q. Li, M. Zhao, L. Y. Bi, Y. Q. Hu, G. Gou, J. Li, Y. Z. Zheng, Two-dimensional silver (I)-dithiocarboxylate coordination polymer exhibiting strong near-infrared photothermal effect. *Inorg. Chem.* 2019, **58**, 6601-6608.

[S16] B. Lü, Y. Chen, P. Li, B. Wang, K. Müllen, M. Yin, Stable radical anions generated from a porous perylenediimide metal-organic framework for boosting near-infrared photothermal conversion. *Nat. Commun.* 2019, **10**, 767.

[S17] Q. Ma, P. Yin, M. Zhao, Z. Luo, Y. Huang, Q. He, Y. Yu, Z. Liu, Z. Hu, B. Chen, H. Zhang, MOF-based hierarchical structures for solar-thermal clean water production. *Adv. Mater.* 2019, **31**, 1808249.